Proceedings Paper:
Nie, L orcid.org/0000-0002-5796-907X, Carpenter, TM, Clegg, HR et al. (3 more authors) (2020) Reducing Dark Region Artifacts in Short-Lag Spatial Coherence (SLSC) Beamforming by Coherence Filtering of the Aperture-Domain Data. In: Proceedings of the 2020 IEEE International Ultrasonics Symposium (IUS). 2020 IEEE International Ultrasonics Symposium (IUS), 07-11 Sep 2020, Las Vegas, NV, USA. IEEE . ISBN 978-1-7281-5449-7

https://doi.org/10.1109/ius46767.2020.9251674

Reducing Dark Region Artifacts in Short-Lag Spatial Coherence (SLSC) Beamforming by Coherence Filtering of the Aperture-Domain Data

Luzhen Nie[1], Thomas M. Carpenter[1], Harry R. Clegg[1], James R. McLaughlan[1,2], David M. J. Cowell[1], and Steven Freear[1]

[1] School of Electronic and Electrical Engineering, University of Leeds, Leeds, U.K.

[2] Leeds Institute of Medical Research, St James' University Hospital, Leeds, U.K.

E-mail: l.nie@leeds.ac.uk and s.freear@leeds.ac.uk

***Abstract*—The short-lag spatial coherence (SLSC) beamformer measures the accumulated similarity of echoes, received by individual transducer elements as a function of spatial separation. It proved beneficial in suppressing incoherent clutter to improve detectability of hypoechoic and anechoic targets. However, with focused beams spatial coherence of backscattered echoes drops significantly away from the focal depth, where dark region artifacts occur due to high-level off-axis interference, reducing the effective depth-of-field when using SLSC. This study aimed to suppress this artificial dropout and keep the image uniformity through depths by filtering the aperture-domain data.**

I. Introduction

The past few decades have witnessed the development of medical ultrasound imaging as a frontline tool in diagnosing a wide range of diseases including cancer [1] and cardiovascular dysfunction [2], [3]. However, suboptimal and inadequate visualization of the anatomy and organ function is still plaguing decision making in clinical practice, especially for difficult-to-image patients associated with obesity [4]. For example, the difficulty of using ultrasound imaging can be seen in many scenarios such as stress echo [5] and abdominal scanning [6], and the problem could be more severe with the dramatically increased rate of obesity. Many factors contribute to poor ultrasound image quality, and of importance are acoustic noise (specular and diffuse reverberations, off-axis scattering, and phase aberration, and so on) and electronic noise (prominent in cases where attenuation is high).

The need of advanced beamforming methods has been recognized in recent years, and exciting progress has been continuously made to combat suboptimal visualization. Spatial-coherence-based reconstruction algorithms have emerged [7]–[10], holding promise in improving detectability of hypoechoic and anechoic targets compared with the conventional delay-and-sum (DAS) beamformer [10]. Among the early efforts, the phase [9] or spectrum [8] of the aperture-domain data (with focusing delays applied) is derived, and a ratio between the coherent and incoherent components is used as a factor to weight DAS images. But 'coherence factors' are easily biased by the increased level of noise, degrading image contrast [11], [12]. Instead, the short-lag spatial coherence (SLSC) beamformer [10], [13] provides image contrast by directly measuring the accumulated similarity of backscattered echoes as a function of element separation. It enables superior contrast-to-noise ratio (CNR) [14] which benefits border delineation in challenging environments with a low signal-to-noise ratio (SNR) [15]. However, with a fixed transmission focus, prefocal dark regions are present mainly in shallow regions of SLSC images, limiting the depth-of-field (DOF) [4]. This study aimed to understand and suppress this artificial dropout.

II. Methods and Materials

A. Conventional SLSC Beamforming

In the context, spatial coherence refers to the similarity of backscattered ultrasound waves that have been sampled by the array at different elements, and the focusing delay has been applied to each channel compensating for path-length differences.

SLSC beamforming uses the accumulated spatial coherence as the direct source of image contrast. For a 1D N-element receive aperture, the calculation of spatial coherence $\hat{R}$ is first performed by using the normalized cross correlation function as given by (1) [10]:

$$\hat{R}(m) = \frac{1}{N-m} \sum_{i=1}^{N-m} \frac{\sum_{n=n_1}^{n_2} s_i(n) s_{i+m}(n)}{\sqrt{\sum_{n=n_1}^{n_2} s_i^2(n) \sum_{n=n_1}^{n_2} s_{i+m}^2(n)}}, \tag{1}$$

where m is the distance, or lag, between two signals on the receive aperture, in the form of number of elements; n is the depth of the beamformed point, in number of samples; $n_1 = n - \frac{K}{2}$ and $n_2 = n + \frac{K}{2}$, where K is the kernel size over which the cross correlation is calculated; s_i and s_{i+m} are the time-delayed signals received by the ith and $(i+m)$th elements, respectively.

Ultrasound backscatters and noise have different characteristics in spatial coherence, and the differences in amplitude between the two are noticeable over a short-lag range. The SLSC metric which integrates the spatial coherence function over the first M lags is defined as (2), to differentiate signals from noise.

$$R_{\text{sl}} = \sum_{m=1}^{M} \hat{R}(m), \tag{2}$$

TABLE I
PARAMETERS FOR FIELD II SIMULATIONS

Parameter	Value
Transducer	Verasonics P4-2v
Transducer pitch	0.3 mm
Elevation focus	60 mm
Transmit aperture	64 elements
Receive aperture	64 elements
Transmit focal depth	60 mm
Center frequency	2.78 MHz
Excitation signal	3-cycle sinusoid
Speed of sound	1540 m/s

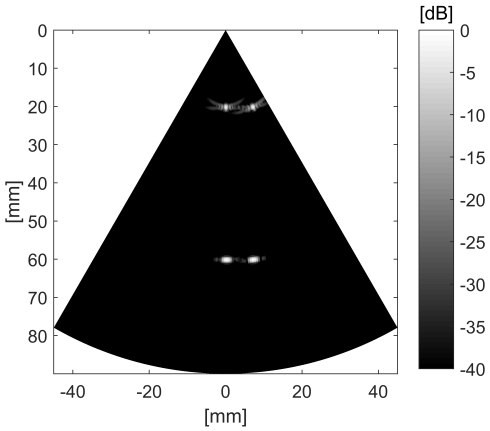

Fig. 1. Field simulations of four scatters with parameters given in Table I. These scatters are located at (0, 20) mm, (7, 20) mm, (0, 60) mm, and (7, 60) mm.

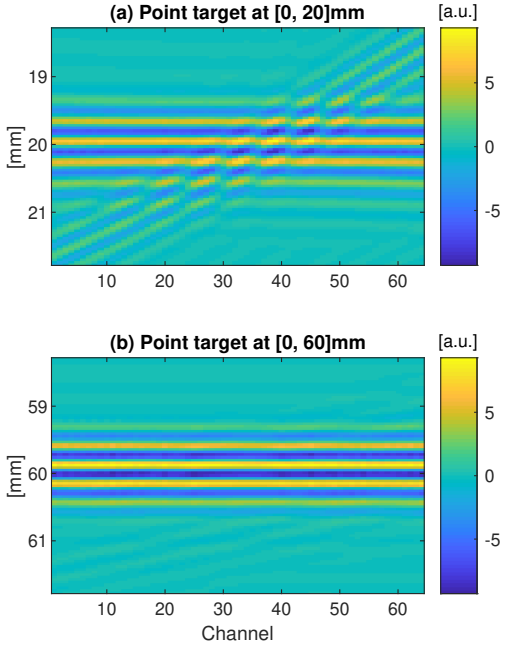

Fig. 2. Delayed wave fields for two point targets located at (0, 20) mm and (0, 60) mm.

where M is the maximum lag. A parameter Q ($Q = M/N$x100%) is introduced and it should be a value between 1% and 30% depending on the specific imaging target and conditions.

B. Field Simulations

At the transmit focus, the spatial coherence can be modeled as the autocorrelation of the aperture for diffuse scatters, with 1 at zero lag and 0 at lag $N - m$. For a point scatter, the spatial coherence function is expected to be constant at 1 for varied lags. Away from the transmit focus, the beam becomes loosely focused and broad. Spatial coherence is altered by the transmit field. A broad beam invalidates the prediction of a coherent wavefront after applying receiving delays, decreasing the spatial coherence of backscattered echoes.

To further elaborate on the potential reasons of the presence of dark region artifacts, point scatters were simulated by Field II [16], [17], with parameters given in Table I. The transmit focus was placed at the depth of 60 mm, matching the elevation focus of the simulated Verasonics P4-2v probe (Verasonics, Inc., WA, USA). As shown in Fig. 1, two pairs of point targets were located at depths of 20 mm and 60 mm, respectively. The differences of point spread functions (PSFs) are visible, where the 'X-shape' sidelobes at 20 mm depth (away from the focal depth 60 mm) are stronger. The aperture-domain data is defined as the data with focusing delays applied but prior to summation. Fig. 2(a) and Fig. 2(b) show the corresponding aperture-domain fields for points located at (0, 20) mm and (0, 60) mm, respectively. Two sets of wavefronts are present in Fig. 2(a), with the coherent one being aligned with the receive aperture and the other one exacerbating spatial coherence. In Fig. 2(b) no strong off-axis interference is visible. This indicates that off-axis scattering originating from broad beam insonification at shallow depths contributes to the increased sidelobe levels and may finally lead to dark region artifacts in SLSC beamforming.

C. Coherence Filtering of the Aperture-Domain Data

Echoes from strong off-axis scatters might dominate in amplitude compared with on-axis echoes. We proposed to interpret the spatial spectrum of the aperture-domain data for suppression of dark region artifacts in SLSC images.

Multiple parallel receive beams can be approximated and reconstructed by the Fourier transform of the aperture-domain data. These beams are centered around the on-axis beam, and distributed equally with an angle step $\Delta \sin\theta = \lambda/(Nd)$, where d indicates the pitch size and λ is the wavelength [8].

Fig. 3 shows the spectrum of the aperture-domain data for the pixel at (0, 20) mm by using a 64-point fast Fourier Transform (FFT), where 64 was equal to the number of elements N. The high-frequency components corresponding to off-axis scattering can be removed (set to zero in linear scale) based on their amplitudes, and the inverse FFT is then used to retract the time domain signal corresponding to the on-axis beam. In this study, high-frequency regions were specified

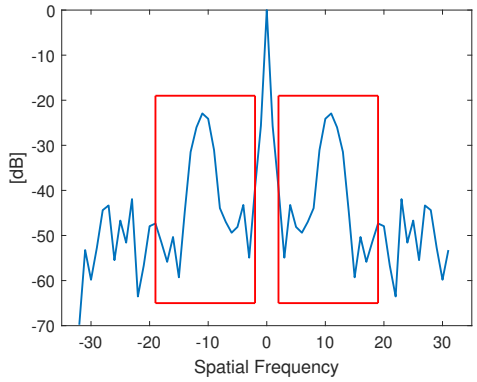

Fig. 3. Spatial spectrum of the aperture-domain data for the pixel at (0, 20) mm. Red lines delineate the high-frequency components which need to be filtered out.

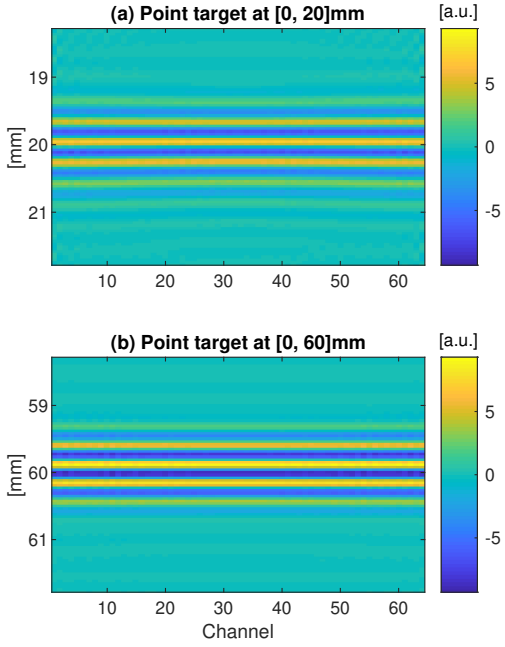

Fig. 4. Filtered wave fields for two point targets located at (0, 20) mm and (0, 60) mm.

by cutoffs M_0 and M_1 (i.e., $[M_0 + 1 : N/2 - M_1 - 1]$ and $[M_1 + 1 - N/2 : -M_0 - 1]$), and they were 1 and 12, respectively. The two corresponding high-frequency regions are delineated by red lines in Fig. 3. The fields shown in Fig. 2 were filtered using this method, with results shown in Fig. 4. It is clear that off-axis scattering in Fig. 2(a) has been removed.

D. Experimental Setup

The Ultrasound Array Research Platform II (UARP II) features a five-level harmonic reduction pulse-width modulation scheme [18]–[21]. It was programmed to scan a CIRS phantom with a Verasonics P4-2v transducer focusing beams at 60 mm (3 cycles @ 2.78 MHz, angle range: -35°: 0.5°: 35°, time gain compensation applied). Prior to SLSC processing, the aperture-domain data for each pixel was first filtered using the method and identical parameters as explained in Section II-C. A kernel size of one wavelength and a maximum lag of 12 ($Q = 19\%$) were heuristically adopted.

E. Experimental Results and Discussion

The generalized CNR (gCNR) [22], which is resistant to dynamic range alteration, was used as a metric for lesion detectability with regions of interest (ROIs) given in Fig. 5(a). This value describes the percentage of pixels that can be resolved from the background. For SLSC, the loss of information away from the focal depth (60 mm) is visible when comparing Fig. 5(b-d). The filtering operation enabled more resolvable pixels in these regions (17% and 28% more for ROI pairs 1 and 2 as shown in Fig. 6). In the nearfield, the transducer-related incoherent reverberations are removed in Fig. 5(c) and Fig. 5(d). Compared with DAS, the filtered SLSC provided higher gCNRs especially for the hypoechoic cyst in ROI pair 2, with 21% more pixels resolved.

SLSC images are particularly suitable for incoherent clutter removal in noisy conditions, but do not necessarily provide improved resolutions. Generally the axial resolution is determined by the correlation kernel size and the lateral resolution is a function of the maximum lag M and SNR [13]. In this work, two fixed cutoffs (M_0 and M_1 in Section II-C) were adopted for all pixels to remove high-frequency portions in the spatial spectrum derived from the aperture-domain data. Automated selection of these cutoffs is a topic of future work, and characterization of the transmit filed could provide meaningful hints.

III. Conclusion

A FFT-based spatial filter was developed to reduce strong off-axis scattering in regions away from the transmit focus. The use of the spatially filtered aperture-domain data led to suppression of dark region artifacts at shallow depths in SLSC images with focused transmissions.

IV. Acknowledgement

L. Nie would like to acknowledge support from the U.K. EPSRC under Grant EP/P023266/1. J. R. McLaughlan's work was supported by an EPSRC Innovation Fellowship EP/S001069/1.

References

[1] M. Abdel-Nasser, J. Melendez, A. Moreno, O. A. Omer, and D. Puig, "Breast tumor classification in ultrasound images using texture analysis and super-resolution methods," *Engineering Applications of Artificial Intelligence*, vol. 59, pp. 84–92, 2017.

[2] M. Cikes, L. Tong, G. R. Sutherland, and J. D'hooge, "Ultrafast cardiac ultrasound imaging: technical principles, applications, and clinical benefits," *JACC: Cardiovascular Imaging*, vol. 7, no. 8, pp. 812–823, 2014.

[3] S. D. Solomon, J. Wu, and L. D. Gillam, *Essential Echocardiography: A Companion to Braunwald's Heart Disease E-Book*. Elsevier Health Sciences, 2017.

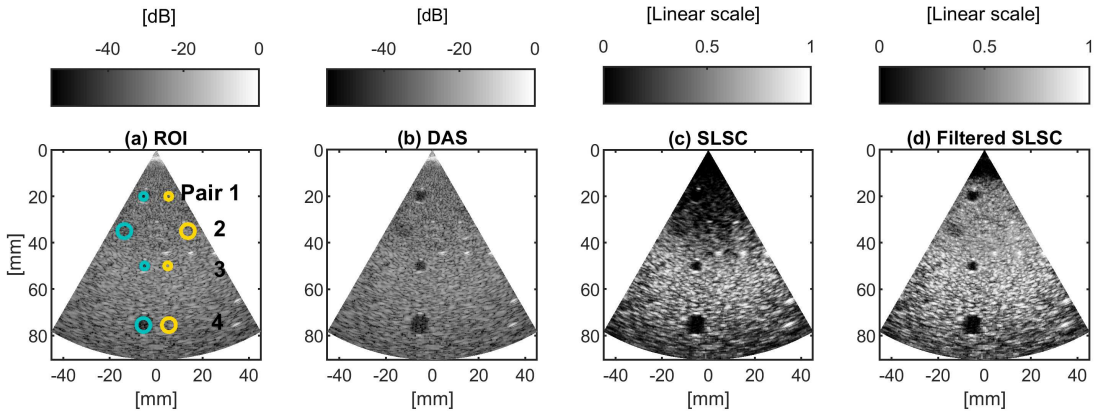

Fig. 5. ROI (a) and images beamformed with DAS (b), SLSC (c) and Filtered SLSC (d). The gCNRs for all ROI pairs as shown in (a) are given in Fig. 6.

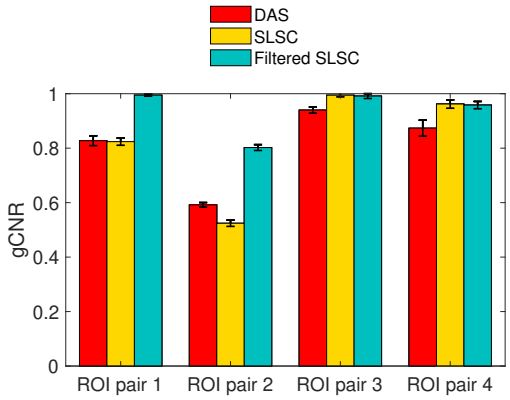

Fig. 6. gCNRs for different ROI pairs when using different beamforming techniques (results shown with the standard deviation error bars based on 10 measurements).

[4] J. J. Dahl, D. Hyun, Y. Li, M. Jakovljevic, M. A. Bell, W. J. Long, N. Bottenus, V. Kakkad, and G. E. Trahey, "Coherence beamforming and its applications to the difficult-to-image patient," in *2017 IEEE International Ultrasonics Symposium (IUS)*. IEEE, 2017, pp. 1–10.

[5] D. Hyun, A. L. C. Crowley, M. LeFevre, J. Cleve, J. Rosenberg, and J. J. Dahl, "Improved visualization in difficult-to-image stress echocardiography patients using real-time harmonic spatial coherence imaging," *IEEE Transactions on Ultrasonics, Ferroelectrics, and Frequency Control*, vol. 66, no. 3, pp. 433–441, 2018.

[6] M. A. Lediju, M. J. Pihl, S. J. Hsu, J. J. Dahl, C. M. Gallippi, and G. E. Trahey, "A motion-based approach to abdominal clutter reduction," *IEEE Transactions on Ultrasonics, Ferroelectrics, and Frequency Control*, vol. 56, no. 11, pp. 2437–2449, 2009.

[7] K. Hollman, K. Rigby, and M. O'donnell, "Coherence factor of speckle from a multi-row probe," in *1999 IEEE Ultrasonics Symposium. Proceedings. International Symposium (Cat. No. 99CH37027)*, vol. 2. IEEE, 1999, pp. 1257–1260.

[8] P.-C. Li and M.-L. Li, "Adaptive imaging using the generalized coherence factor," *IEEE Transactions on Ultrasonics, Ferroelectrics, and Frequency Control*, vol. 50, no. 2, pp. 128–141, 2003.

[9] J. Camacho, M. Parrilla, and C. Fritsch, "Phase coherence imaging," *IEEE Transactions on Ultrasonics, Ferroelectrics, and Frequency Control*, vol. 56, no. 5, pp. 958–974, 2009.

[10] M. A. Lediju, G. E. Trahey, B. C. Byram, and J. J. Dahl, "Short-lag spatial coherence of backscattered echoes: Imaging characteristics," *IEEE Transactions on Ultrasonics, Ferroelectrics, and Frequency Control*, vol. 58, no. 7, pp. 1377–1388, 2011.

[11] H. Hasegawa and H. Kanai, "Effect of subaperture beamforming on phase coherence imaging," *IEEE Transactions on Ultrasonics, Ferroelectrics, and Frequency Control*, vol. 61, no. 11, pp. 1779–1790, 2014.

[12] M. Xu, X. Yang, M. Ding, and M. Yuchi, "Spatio-temporally smoothed coherence factor for ultrasound imaging [correspondence]," *IEEE Transactions on Ultrasonics, Ferroelectrics, and Frequency Control*, vol. 61, no. 1, pp. 182–190, 2014.

[13] M. A. L. Bell, J. J. Dahl, and G. E. Trahey, "Resolution and brightness characteristics of short-lag spatial coherence (slsc) images," *IEEE Transactions on Ultrasonics, Ferroelectrics, and Frequency Control*, vol. 62, no. 7, pp. 1265–1276, 2015.

[14] E. Pozo, B. Castañeda, J. Dahl, and R. Lavarello, "A comparison between generalized coherence factor and short-lag spatial coherence methods," in *2015 IEEE 12th International Symposium on Biomedical Imaging (ISBI)*. IEEE, 2015, pp. 231–234.

[15] J. J. Dahl, D. Hyun, M. Lediju, and G. E. Trahey, "Lesion detectability in diagnostic ultrasound with short-lag spatial coherence imaging," *Ultrasonic Imaging*, vol. 33, no. 2, pp. 119–133, 2011.

[16] J. A. Jensen, "Field: A program for simulating ultrasound systems," in *10TH NORDICBALTIC CONFERENCE ON BIOMEDICAL IMAGING, VOL. 4, SUPPLEMENT 1, PART 1: 351–353*. Citeseer, 1996.

[17] J. A. Jensen and N. B. Svendsen, "Calculation of pressure fields from arbitrarily shaped, apodized, and excited ultrasound transducers," *IEEE Transactions on Ultrasonics, Ferroelectrics, and Frequency Control*, vol. 39, no. 2, pp. 262–267, 1992.

[18] E. Boni, C. Alfred, S. Freear, J. A. Jensen, and P. Tortoli, "Ultrasound open platforms for next-generation imaging technique development," *IEEE Transactions on Ultrasonics, Ferroelectrics, and Frequency Control*, vol. 65, no. 7, pp. 1078–1092, 2018.

[19] D. M. Cowell, P. R. Smith, and S. Freear, "Phase-inversion-based selective harmonic elimination (pi-she) in multi-level switched-mode tone- and frequency-modulated excitation," *IEEE Transactions on Ultrasonics, Ferroelectrics, and Frequency Control*, vol. 60, no. 6, pp. 1084–1097, 2013.

[20] P. R. Smith, D. M. Cowell, and S. Freear, "Width-modulated square-wave pulses for ultrasound applications," *IEEE Transactions on Ultrasonics, Ferroelectrics, and Frequency Control*, vol. 60, no. 11, pp. 2244–2256, 2013.

[21] D. Cowell and S. Freear, "Quinary excitation method for pulse compression ultrasound measurements," *Ultrasonics*, vol. 48, no. 2, pp. 98–108, 2008.

[22] A. Rodriguez-Molares, O. M. H. Rindal, J. D'hooge, S. Måsøy, A. Austeng, M. A. Lediju Bell, and H. Torp, "The generalized contrast-to-noise ratio: A formal definition for lesion detectability," *IEEE Transactions on Ultrasonics, Ferroelectrics, and Frequency Control*, vol. 67, no. 4, pp. 745–759, 2020.